Analysis of heat and mass transfer limitations for the combustion of methane emissions on PdO/Co3O4 coated on ceramic open cell foams

Analysis of heat and mass transfer limitations for the combustion of methane emissions on PdO/Co_3O_4 coated on ceramic open cell foams

Carmen W. Moncada Quintero[1]*, *Giuliana Ercolino*[1], *Abhinav Poozhikunnath*[2,3], *Radenka Maric*[2,3], *Stefania Specchia*[1]*

[1] Politecnico di Torino, Department of Applied Science and Technology, Corso Duca degli Abruzzi 24, 10129 Torino, Italy

[2] University of Connecticut, Department of Materials Science and Engineering, 97 North Eagleville Road, Storrs, CT 06269, USA

[3] University of Connecticut, Center for Clean Energy Engineering, 44 Weaver Road, Storrs, CT, 06269-5233, USA

* Corresponding authors: carmen.moncada@polito.it, stefania.specchia@polito.it

Graphical Abstract

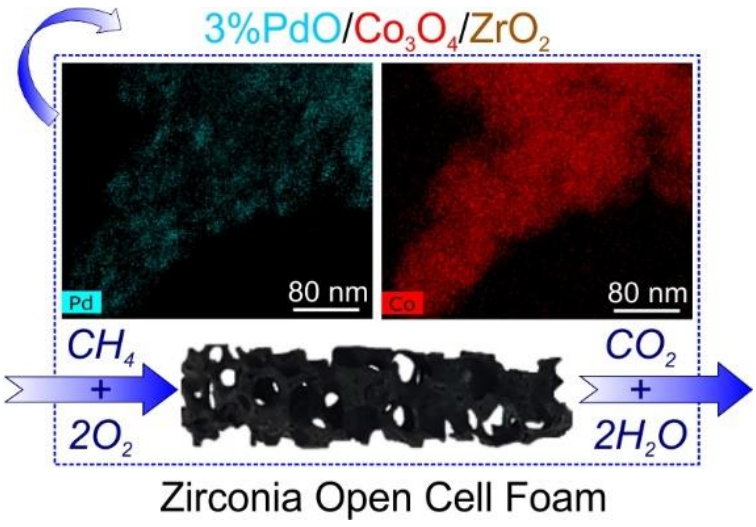

Keywords

Structured catalysts; ceramic open cell foams; mass/heat transfer effects; thermal conductivity; stability; PdO dispersion.

Highlights

- 3% PdO/Co_3O_4 coated on alumina, silicon carbide, and zirconia open cell foams.
- Best catalytic activity belongs to zirconia open cell foam coated with 200 mg on Co_3O_4.
- Importance of the low thermal conductivity of the foam to favor the catalytic reaction.
- Catalytic activity decreases slightly after 250 hours of time on stream.
- STEM analysis for PdO dispersion on fresh/aged zirconia open cell foams.

Abstract

Coated ceramic open cells foams (OCFs) with catalysts offer an attractive alternative to packed bed reactors for process intensification. Here, the effect of 3 wt.% PdO on Co_3O_4 coated on three different OCF (alumina, silicon carbide and zirconia) was investigated toward the reaction of CH_4 combustion in lean conditions. The OCFs were characterized by Raman spectroscopy and FESEM analysis. The operating regime of each OCF catalyst was investigated using a series of mass transfer resistances assuming pseudo first order reaction (large excess of oxygen). The thermal conductivity of OCF plays an important role on the overall performance of the combustion reaction in terms of heat and mass transfer. The best OCF structured catalyst was tested up to 250 hours of time-on-stream, demonstrating good stability. PdO dispersion over the structured catalyst at the fresh and aged status was assessed by STEM analysis.

1. Introduction

Global warming is one of the most serious environmental threats facing the world today. Greenhouse gases (GHGs) such as carbon dioxide (CO_2), methane (CH_4), and nitrous oxide (N_2O) are the main factors responsible for greatly warming the surface of the Earth [1]. Transportation sector is one of the largest sources of GHG emissions [2]. Globally, about 27% of man-made CO_2 emissions come from burning fossil fuel produced by motor vehicles (mainly internal combustion engines) [3]. Natural gas (primarily composed of CH_4) is the most attractive and clean burning alternative transportation fuel to reduce environmental pollution since it emits the lowest CO_2 emissions, less NO_x, and particulates in the exhaust compared to gasoline and diesel engines [4]. In addition, natural gas engines can operate at lean-burn conditions, minimizing the typical products of incomplete combustion in comparison to stoichiometric conditions [3]. However, these advantages are in part offset by the emissions of unburned CH_4 in the exhaust gases.

Catalytic converters are an efficient technology to reduce CH_4 emissions, via a catalytic oxidation at low temperature [5]. Pd-based catalysts have been reported to be the most active catalytic systems for the total oxidation of CH_4, due to their high activity at low temperature [6–9]. However, due to the relatively high cost associated with palladium, researchers have paid much attention to the study of different alternative systems such as oxides or mixed oxides [10–12] and perovskites [13–15] supporting Pd. In all cases, catalytic properties of supported Pd catalysts depend on the nature of catalyst carrier as well as active phase-support interaction [6,9,16,17].

Today, scientists focus the attention on structured catalysts for process intensification [18–23]. In particular, monolith- and foam-based catalysts offer a series of advantages compared to classical fixed beds with pellets [24], such as higher superficial geometric area (surface/volume ratio, $m^2\ m^{-3}$), higher thermal stability, higher porosity, and tortuosity, an homogeneous

structure able to guarantee constant characteristics over a wide range of operative conditions. Thus, monolith- and foam-based structured catalysts offer lower pressure drop and higher space velocity while in operation, allowing for a reduction of the catalyst loading [18–23].

In particular, OCFs are already available on the market and represent a valid and economic alternative to ceramic monoliths[25–30][25–30][25–30][25–30][25–30][25–30]. To our knowledge, OCFs are commercially used in many different applications, such as filters for foundry industry and aluminum production, filters for hot gases or liquids in petrochemical and food industry, thermal insulators or heat exchangers in mechanical and construction sectors, and bone substitute for implants in biomedical applications [25–30]. No commercial applications are yet implemented in the catalysis sector. Indeed, there are many research groups, our included, which are focusing their research efforts on ceramic and metallic OCFs as supports for catalysts in many different chemical reaction, such as reforming of methane and biogas [31,32], partial and total oxidation of methane [33,34], CO and VOC oxidation [35,36], and many other applications in chemical reactor engineering [19,37–39]. Thus, OCFs represent a viable and potential substitute of commercially available monoliths, and the research in this field is growing fast.

The reduction of Pd content in supported Pd-based catalysts while maintaining or improving the catalytic activity is another important research target for a more economical process. On this purpose, transition metal oxides constitute probably one of the most interesting supports in many catalytic reactions such as oxidation of CO [40,41], activation of hydrocarbons [42,43], and reduction of NO_x [44,45]. Among all the transition metal oxides, spinel cobalt oxide (Co_3O_4) represents a promising transition oxide catalyst for the total oxidation of methane in combination with Pd [10,46,47], mainly due to its high surface oxide mobility [48,49].

The main objective of this work is to evaluate the impact of the different ceramic OCF materials coated with a 3 wt.% PdO/Co_3O_4 on mass and heat transport for the complete methane

combustion in lean conditions. Possible applications can be envisaged in the removal of unburnt CH_4 in the automotive sector, or process intensification for environmental cleaning. This specific catalyst composition was selected from our previous optimization works performed on PdO/Co_3O_4 at powder lever, in terms of PdO amount and best conditions of synthesis [46,47,50]. The PdO/Co_3O_4 catalyst was deposited on ceramic OCF of various compositions (alumina, silicon, carbide, and zirconia) via a two-steps synthesis: first, solution combustion synthesis (SCS) of the Co_3O_4 spinel on the OCFs, and second, wetness impregnation (WI) of 3 wt.% Pd on the Co_3O_4 spinel, according to our previous optimizations [46,47,50]. The SCS is a well-known and user-friendly method for preparing structured catalysts in a fast and cheap way by mixing metal nitrate precursors with an organic fuel [34,51–54]. Moreover, SCS is an easily scalable technique in the case of possible large-scale production for process intensification [55,56]. The catalytic activity of the all OCF catalysts was tested towards the lean CH_4 combustion by varying the inlet CH_4 concentration (0.5 and 1.0 vol.%), by maintaining constant the CH_4/O_2 molar ratio, equal to 8, and at WHSV of 30 NL h^{-1} g_{cat}^{-1}. Mass and heat transfer effects were evaluated at the inlet CH_4 concentration of 0.5 vol.% for all the OCF catalysts. The most promising support for PdO/Co_3O_4 catalyst toward CH_4 combustion was selected to investigate the stability of the catalyst after approximately 250 h of operative time of stream [57]. All coated structures were characterized form the chemical point of view via Raman spectroscopy. The morphology of the catalysts was analyzed by field emission scanning electron microscopy (FESEM) and scanning transmission electron microscopy (STEM) techniques.

2. Materials and methods

2.1. Open cell foams and Chemicals

Zirconia OCF (Vukopor® HT30, labelled Zir-OCF), alumina OCF (Vukopor® A30, labelled Alu-OCF), and silicon carbide OCF (Vukopor® S30, labelled SiC-OCF) of 30 ppi (pore per inch) were purchased from Lanik s.r.o. (Czech Republic, [26]). The OCFs were of 30 mm length and 9 mm diameter.

All the reagents were purchased from Sigma–Aldrich: cobalt(II) nitrate hexahydrate $Co(NO_3)_2 \cdot 6H_2O$ (≥98% purity), palladium(II) nitrate hydrate $Pd(NO_3)_2 \cdot xH_2O$ (≥99% purity), glycine NH_2CH_2COOH (≥99% purity), ethanol CH_3CH_2OH (≥99.8% purity), isopropyl alcohol $(CH_3)_2CHOH$ (≥98% purity), and propanone CH_3COCH_3 (≥99.8% purity). Aqueous solutions were prepared using ultrapure water obtained from a Millipore Milli-Q system with a resistivity ≈ 18 MΩ cm. For catalytic activity tests, pure methane, oxygen, and nitrogen (purity 99.999%) were supplied in cylinders provided by SIAD S.p.A.

2.2. Preparation of the structured catalysts

Before use, all OCFs were cleaned in water/propanone (50/50 vol.%) ultrasonic bath for 30 min at room temperature and dried at 250 °C for 60 min. Then, according to our previous optimization described in Ercolino et al. [33,34,46], 200 mg of Co_3O_4 catalyst was deposited on all OCFs by the SCS method. The coating procedure, which was repeated till the desired spinel loading was achieved, consisted of immersion of each OCF in a solution of cobalt nitrate and glycine (cobalt nitrate/glycine stoichiometric ratio of 0.25), removal of the excess of solution with a flow of compressed air, and SCS reaction step in a furnace at 250 °C for 15 min. As the last step, all OCFs were calcined for 4 h at 600 °C in calm air.

Then, 3 wt.% PdO was deposited by WI, from a 3 M solution of Pd nitrate, by repeating the impregnation several times till reaching the desired amount, followed by a further calcination of 4 h at 600 °C in calm air, as described in our previous works [33,34,46].

2.3. Adherence tests

Sonication was used to mechanically stress the coated OCF and verify the adhesion of the coated catalyst to the ceramic structures, according to our previous works and the literature [47,58,59]. The coated foams were immersed in a 50/50 solution of water/isopropanol and sonicated at 40 kHz, 130 W, for 2 hours (S3M 2200 device by Sonica). The OCF were weighted before and after sonication treatment (after 30 min drying in a static oven at 120 °C), to evaluated the loss of weight after sonication.

2.4. Catalytic Tests toward CH_4 combustion

A series of catalytic tests was performed by evaluating the activity of the three different OCF materials (3 wt.% PdO on 200 mg Co_3O_4 on Alu-OCF, SiC-OCF, and Zir-OCF, respectively) toward CH_4 combustion, feeding 0.5 vol.% CH_4 and 4 vol.% O_2 in N_2, or 1.0 vol.% CH_4, and 8 vol.% O_2 in N_2, as inlet concentration (O_2/CH_4 molar ratio of 8, lean conditions, in both series of tests). A fixed bed reactor consisting of a straight quartz tube, 10 mm ID, placed into a PID-regulated electrical oven, was used to this purpose. To avoid channeling phenomena, all OCFs were wrapped with a vermiculite foil to perfectly fit the cross section of the microreactor. The WHSV was set at 30 NL h^{-1} g_{cat}^{-1}.

All catalytic tests were performed according to the procedure described in detail in Ercolino et al. [33,34]. After heating the reactor up to 700 °C at 10 °C min^{-1} while feeding the reactive gas mixture, and reached steady state conditions (that is, full conversion of CH_4), the reactor was cooled to room temperature (5 °C min^{-1}) while monitoring the reactor outlet dry gas concentrations as a function of temperature (measured by a K-type thermocouple placed few mm inside the inlet side of the OCF). An online analyzer (ABB Company) equipped with an NDIR module Uras 14 for $CO/CO_2/CH_4$, and a paramagnetic module Magnos 106 for O_2, was used on purpose. The data collected from the online analyzer were elaborated and analyzed to draw CH_4 conversion as a function of the temperature. Each catalytic test was repeated at least

three times, and the average values among the three tests are reported (standard deviation below 3%).

2.5. Stability measurements

A catalytic test was performed on the best-selected OCF catalyst, while maintaining constant inlet CH_4 concentration of 0.5 vol.% (O_2/CH_4 molar ratio equal to 8) and WHSV of 30 NL h^{-1} g_{cat}^{-1}, with the main purpose of verifying the stability of the best catalyst [57]. The reaction was initially run for five consecutive days at 400 °C, and again for another five consecutive days at 400 °C after two days resting at room temperature. The catalytic activity of the best-performing OCF catalyst was evaluated as described previously, at the beginning and at the end of the stability test (fresh/aged conditions), after approximately 250 h of operative time of stream.

2.6. External and Internal Mass Transfer Limitations

In order to study the internal (inside the pore of the catalyst layer) and external (gas film surrounding the structured catalyst) mass transfer effects, a series of resistances have been considered to evaluate the operating regime of each OCF catalyst. The total resistance to mass transfer (${R_m}^t$) can be expressed as the sum of two diffusive resistance contributions (using a series approach) [60–63]:

$$ {R_m}^t = {R_m}^e + {R_m}^i \quad (1) $$

$$ {R_m}^t = \frac{1}{{k_m}^t} \; ; {R_m}^e = \frac{1}{{k_m}^e} \; ; \; {R_m}^i = \frac{1}{{k_m}^i} \quad (2) $$

where ${R_m}^e$ is the resistance due to the external mass transfer between the bulk of the gas phase and the outer surface of the Pd/Co_3O_4 catalyst layer (m); ${R_m}^i$ is the resistance due to mass transfer within the Pd/Co_3O_4 catalyst layer (m); ${k_m}^t$, ${k_m}^e$, and ${k_m}^i$ are the total, external and internal mass transfer coefficients (m s^{-1}), respectively.

For solid OCF, the external mass transfer coefficient (${k_m}^e$) can be estimated according to Garrido et. al. [64] as:

$$ Sh_{OCF} = 1.0 \cdot Re^{0.47} \cdot Sc^{\frac{1}{3}} \cdot F_g \quad (3) $$

$$k_m{}^{e} = \frac{Sh_{OCF} \cdot D_f}{4 \cdot R_{\Omega e}} \quad (4)$$

$$Re_{OCF} = \frac{d_{p,c} \cdot u \cdot \rho_f}{\mu_f} \; ; \; Sc = \frac{\mu_f}{\rho_f \cdot D_f} \; ; \; F_g = \left(\frac{d_{p,c}}{0.001}\right)^{0.58} \varepsilon_{ocf}^{0.44} \quad (5)$$

where Sh_{OCF} is the external Sherwood number for solid OCF, Re is the Reynold number, Sc is the Smith number, F_g is the geometrical factor which depends on the pore diameter ($d_{p,c}$) and the voidage (ε_{ocf}) of the OCF, D_f is the molecular diffusivity of CH_4 in gas mixture ($m^2\ s^{-1}$), $R_{\Omega e}$ is the characteristic length scale for transverse diffusion associated within gas phase (m) calculated as the ratio of the flow area $A_{\Omega,e}$ to the gas–coated layer interfacial perimeter (P_Ω), u is the inlet gas velocity at operative conditions ($m\ s^{-1}$), ρ_f is the density of gas mixture ($kg\ m^{-3}$), and μ_f is the viscosity of gas mixture ($kg\ m^{-1}\ s^{-1}$). The correlation for the estimation of the dimensionless mass transfer coefficient Sh_{OCF} (Eq. 3) is valid for the range of OCF voidage of $0.75 \leq \varepsilon_{ocf} \leq 0.85$ and cell diameter of $0.87 \leq d_{p,c} \leq 3.13\ mm$.

The internal mass transfer coefficient ($k_m{}^{i}$) can be estimated according to the correlation proposed by Joshi et al. [61]:

$$Sh_c = Sh_{c,\infty} + \frac{\Lambda \cdot \phi^2}{1 + \Lambda \cdot \phi} \quad (6)$$

$$k_m{}^{i} = \frac{Sh_c \cdot D_e}{R_{\Omega,i}} \quad (7)$$

where Sh_c is the internal Sherwood number, $Sh_{c,\infty}$is the asymptotic internal Sherwood number ($Sh_{c,\infty} = 3.013$ for circular pore diameter and coated layer shape) [65,66], ϕ is the Thiele modulus, Λ is a constant that depends on the coated layer geometric and kinetic parameter for a first order reaction ($\Lambda = 0.38$ for a circular coated layer shape with circular crown ratio of 1.01) [60,61], D_e is the effective diffusivity of CH_4 in the coated layer ($m^2\ s^{-1}$), and $R_{\Omega,i}$ is the characteristic length scale for the coated catalyst layer (m) [60–63,66] calculated as the ratio of coated cross-sectional area ($A_{\Omega,i}$) to the gas-coated layer interfacial perimeter (P_Ω). Since the reaction under consideration (complete combustion of methane) is carried out in a large excess

of oxygen $C_{O_2} \gg C_{CH_4}$ (lean conditions), the kinetic can be approximated as a pseudo-first order reaction:

$$CH_4 + 2O_2 \rightarrow CO_2 + 2H_2O \tag{8}$$

$$R^{obs} = k \cdot C_{CH_4} \tag{9}$$

where R^{obs} is the observed reaction rate expressed with respect to methane (mol m^{-3} s^{-1}) and k is the apparent first order reaction rate constant (s^{-1}) which was determined by the Arrhenius equation (see Eq. 10) using the experimental data points with methane conversion lower than 10% :

$$k = A_o \cdot e^{-\frac{E_{app}}{R_g \cdot T}} \tag{10}$$

where A_o is the pre-exponential factor (s^{-1}), E_{app} is the apparent activation energy of the combustion reaction (J mol^{-1}), R_g is the universal gas constant (J mol^{-1} K^{-1}) and T is the absolute temperature (K).

To describe the relationship between diffusion and reaction rate in porous catalyst with no mass transfer limitations, the Thiele modulus (ϕ) for a first order reaction was determined by the following expression [60–62,65–68]:

$$ø = \sqrt{\frac{k \cdot {R_{\Omega i}}^2}{D_e}} \tag{11}$$

If the Thiele modulus is large ($\gg 1$, fast reaction), the conversion of the combustion process is controlled by diffusion, while if the Thiele modulus is small ($\ll 1$, slow reaction), the conversion is controlled by chemical reaction.

The effectiveness factor (η) was calculated using the analytical solution for cylindrical geometry for first order reaction as [60–62,65,67]:

$$\eta = \frac{1}{\phi} \cdot \frac{I_1(2\phi)}{I_0(2\phi)} \tag{12}$$

where I_0, I_1 are the zero and first order modified Bessel functions of the first kind, respectively. For slow reaction the effectiveness factor $\eta \to 1$ and fast reaction $\eta \to \frac{1}{\phi}$.

2.7. External and Internal Heat Transfer Limitations

In addition to mass transfer effects, heat transfer limitations can also occur in heterogeneous catalysis, in particular for strongly exothermic reactions such as the complete combustion of methane. Temperature gradients can be originated within the catalytic layer (internal heat transfer) or more frequently, between the bulk of the gas phase and the surface of the catalyst (external heat transfer) which lead to the catalyst deactivation due to the thermal sintering. For that, heat management in chemical reactions is of vital importance for both reactor design and control of the overall process.

The interphase heat transfer limitations can be evaluated using the criterion derived by Mears in 1971 [69] using the perturbation approach, in which the heat transfer resistance of the fluid phase is assumed to be lumped at the surface:

$$\chi = \left|\frac{(-\Delta H_r)\cdot R^{obs}\cdot R_{\Omega e}}{h_e \cdot T_b}\right| < \frac{0.15}{\gamma_b}; \tag{13}$$

$$\gamma_b = \frac{E_{app}}{R_g \cdot T_b} \tag{14}$$

where ΔH_r is the heat of methane combustion reaction (J mol^{-1}), h_e is the heat transfer coefficient associated for the gas phase (W m^{-2} K^{-1}), T_b is the temperature in the bulk of the gas phase (K); γ_b is the Arrhenuis number evaluated at the bulk of the gas phase, R_g is the universal gas constant (J mol^{-1} K^{-1}), and χ is the Damkholer for interphase heat transport [65,67–71].

Concerning the intraparticle heat transfer effects, the thermal gradients inside the catalyst layer can be assumed absent according to the Anderson's criterion proposed in 1963 as [72]:

$$\psi = \left|\frac{\left(-\Delta H_r \cdot R^{obs} \cdot R_{\Omega i}^2\right)}{\lambda_e \cdot T_s}\right| < \frac{0.75}{\gamma_s}; \quad (15)$$

$$\gamma_s = \frac{E_{app}}{R_g \cdot T_s} \quad (16)$$

where λ_e is the effective thermal conductivity (W m^{-1} K^{-1}), T_s is the temperature at the surface of the catalyst layer (K), γ_s is the Arrhenuis number evaluated at the surface of the gas phase, and ψ is the Damkohler for intraparticle heat transport [65,67,68,70–72].

Under steady state conditions, the heat released by the methane combustion reaction (Q_r) on any element of the outer PdO/Co_3O_4 catalyst surface must be transported from the solid catalytic thickness to the bulk fluid. Assuming pseudo-first order reaction the steady state analysis is given as [67]:

$$Q_r = Q \quad (17)$$

$$Q_r = \left(R'_{CH4}\right) \cdot \left(-\Delta H_r\right) = A'_o \cdot e^{\left(-\frac{\gamma_b}{\theta+1}\right)} \cdot C_{CH4} \cdot \left(-\Delta H_r\right) \quad (18)$$

$$Q = h_e \cdot a_m \cdot \left(T_s - T_b\right) = h_e \cdot a_m \cdot T_b \cdot \theta \quad (19)$$

where Q_r is the rate of heat generation per unit mass of catalyst (J Kg^{-1} s^{-1}), Q is the rate of heat removal per unit mass of catalyst (J Kg^{-1} s^{-1}), R'_{CH4} is the reaction rate expressed with respect to methane per unit mass of catalyst (mol Kg^{-1} s^{-1}), A'_o is the pre-exponential factor per unit of the catalyst bulk density (m^3 Kg^{-1} s^{-1}), a_m is the external surface area per unit mass of catalyst (m^2 Kg^{-1}), and θ is the dimensionless temperature defined by Eq. 20:

$$\theta = \frac{T_s - T_b}{T_b} \quad (20)$$

2.8. Physical-Chemical Characterization

The chemical composition of the 3% PdO/Co_3O_4 catalyst coated on all OCF was analyzed via Raman spectroscopy with a Micro-Raman instrument (Renishaw plc, Wottonunder-Edge, UK,

equipped with a cooled CCD camera with an excitation wavelength of 514 nm). The Raman scattered light was collected in the spectral range 200–1000 cm^{-1}. Twelve scans per measurements were accumulated to ensure a sufficient signal-to-noise ratio.

The morphology and homogeneity of the catalytic coating was investigated on Zir-OCF via field-emission scanning electron microscopy (FESEM, JEOL-JSM-6700F).

The specific surface areas (S_{BET}) of the coated ceramic foams were measured by nitrogen physisorption at –196 °C using a Micromeritics ASAP 2020 instrument. The measurements were performed by inserting small pieces of the foams into the burette, and outgassing overnight at 150 °C in low vacuum (10 Pa). The S_{BET} were evaluated by the Brunauer–Emmett–Teller method between 0.05 and 0.30 p/p°.

PdO dispersion on Co_3O_4 coated on Zir-OCF was evaluated before and after the stability test on the fresh and aged structured catalyst by scanning transmission electron microscopy (STEM, 200kV Talos F200X FEG S/TEM) coupled with energy dispersive X-ray spectroscopy (EDXS) mapping. The specimens for STEM analysis were prepared by cutting a few pieces of catalyst coated material from the Zir-OCF and dispersing it in ethanol by sonication and adding one drop of the dispersed mixture on to a 3 mm Cu grid with holey carbon film (Pacific Grid-Tech). The specimens were covered and allowed to dry overnight at room temperature before they were analyzed.

3. Results and Discussion

3.1. Physical-Chemical Characterization

Table 1 summarizes the textural and geometrical properties of the three bare 30 ppi OCFs, evaluated according to Buciuman and Kraushaar-Czarnetzki [73]. Section **S.1** of the *Supporting Info* (***S.1.*** *Estimation of the textural and geometrical properties of the OCF*) explains all the equations used to obtain the values listed in **Table 1**, as reported in our previous works [33,34].

Notwithstanding the same pore per inch values of the three types of OCFs, the textural properties are very different. For example, the average pore dimension increases in the order Zir-OCF < Alu-OCF < SiC-OCF, while the geometric surface area and surface area decreases in the order Zir-OCF > Alu-OCF > SiC-OCF. Instead, in terms of voidage, Zir-OCF has the lowest value, whereas the Alu-OCF and SiC-OCF are very similar, slightly higher values. In addition, the thermal conductivity is very different, increasing in the order Zir-OCF < Alu-OCF < SiC-OCF. The S_a values are very low, equivalent to a specific surface area of approx. 0.002 $m^2\ g^{-1}$. The S_a values listed in **Table 1** have been calculated by applying the formula of Buciuman and Kraushaar-Czarnetzki [73], considering the strut of the foam as a dense package of single tetrakaidekahedron (all the formula employed are listed in the section **S.1** of the *Supporting Info*). Because of these low values of S_a, and considering that OCFs can be porous with additional internal void volume due to the fabrication process, measuring the S_{BET} on bare OCFs via conventional physisorption methods has no practical meaning [64,74].

Table 1. Textural and geometrical properties of the three 30 ppi OCFs.

Bare OCF	**Zir-OCF**	**Alu-OCF**	**SiC-OCF**
Average pore dimension, d_p [mm]	1.30 ± 0.73	1.34 ± 0.55	1.63 ± 0.65
Average strut thickness, t_s [mm]	0.47 ± 0.16	0.34 ± 0.10	0.42 ± 0.16
Face diameter, d_f [mm]	1.77	1.68	2.05
Foam relative density, ρ_r [-]	0.183	0.106	0.109
Voidage, ε [-]	0.817	0.894	0.891
Geometric surface area, S_{ga} [mm^{-1}]	1.164	0.934	0.776
Surface area, S_a [mm^2]	2221	1783	1480
Thermal condictivity, λ_f [$W\ m^{-1}\ K^{-1}$]	0.027 [75]	0.16 [76]	0.40 [77]

From the adherence tests performed by sonication, the adherence values span from 98.3 to 98.8 wt.%, showing a strong interaction of the catalytic layer with the walls of the structures, independently of the nature of the ceramic foams. These values, with an overall loss of catalyst slightly higher than 1 wt.%, are matching very well with our previous adherence results on ceramic and metallic foams [23,34,58] and also with literature values on ceramic and metallic foams [22,78]

Figure 1 shows pictures and FESEM images at low and high magnification of Zir-OCF, in the bare and coated status (3% Pd on 200 mg Co_3O_4). The surface of the bare OCF is flat, confirming the low S_{BET} values measured, while the surface of the coated OCF is rather rough, thanks to the gasses released during the SCS reaction [54,55]. The catalytic layer results homogeneously distributed all along the structure, and very well anchored, with an average thickness of around 55 ± 15 μm. This value is in line with the values reported in the open literature for similar structures, both monoliths and foams [55,58,79,80]. Very similar morphology and thicknesses were observed also for Alu-OCF and SiC-OCF (not shown here). The S_{BET} values measured on the three coated foams (adsorption/desorption curves not reported here) were very similar among them ranging from 4.6 to 5.0 $m^2\ g^{-1}$, various orders of magnitude higher than the specific surface area values of the bare OCFs. These values are typical of the Pd/Co_3O_4 S_{BET} values in powder, which is equal to 5.1 $m^2\ g^{-1}$, for 3% PdO deposited over Co_3O_4, as we evaluated experimentally in one of our previous works [47]. Thus, even if the starting ceramic materials are different, and with very low specific area (see S_a values in **Table 1**), we can affirm that their low and almost equal *Sa* values do not influence the nature and morphology of the catalyst lined on the bare OCFs when we move from powder to structured ones, being the morphological characteristic of the coated PdO/Co_3O_4 deposited over the foams the same of the powder Pd/Co_3O_4. We got similar results by lining a different catalyst ($Ru/La\text{-}Al_2O_3$) either on ceramic and metallic monoliths [23,81]. Thus, we can conclude that the coating

process allows us obtaining ceramic OCFs with a high specific surface area, which depends exclusively on the nature of the catalyst coated over.

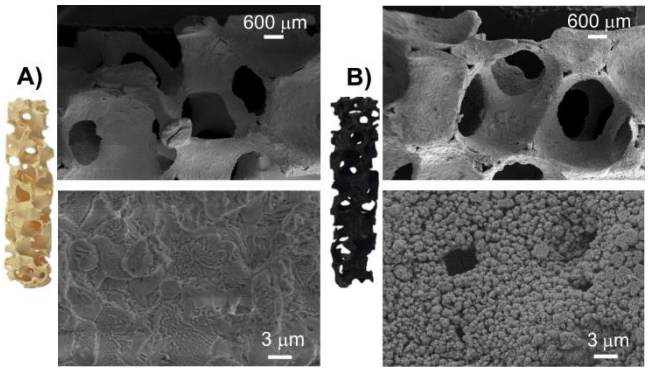

Figure 1. 30 ppi Zir-OCF used in this work: **A)** bare structure, and **B)** coated structure with 3 wt,% PdO/Co_3O_4. FESEM images at 40X and 10,000X magnification.

Figure 2.2 shows Raman spectra of the three coated 30 ppi OCFs. All recorded spectra are almost identical, sign that the SCS method allowed coating the catalyst maintaining its chemical characteristics on the three different structures, independently of their nature (zirconia, alumina, or silicon carbide). The lines located at 487, 526, 624, and 694 cm^{-1}, respectively, correspond to the E_g, $2xF_{2g}$, and A_{1g} vibrational modes of crystalline Co_3O_4 spinel [82,83], confirming definitely its presence in all structured catalysts. The spectra of the structured catalysts are almost coincident with the Raman spectra obtained for PdO/Co_3O_4 synthesized as a powder in our previous studies [46]. Raman spectra of PdO, expected at around 467, 640, and 680 cm^{-1} (E_g and B_{1g} vibrational modes) [46,84], cannot be distinguished clearly because of the relatively low concentration of PdO [46].

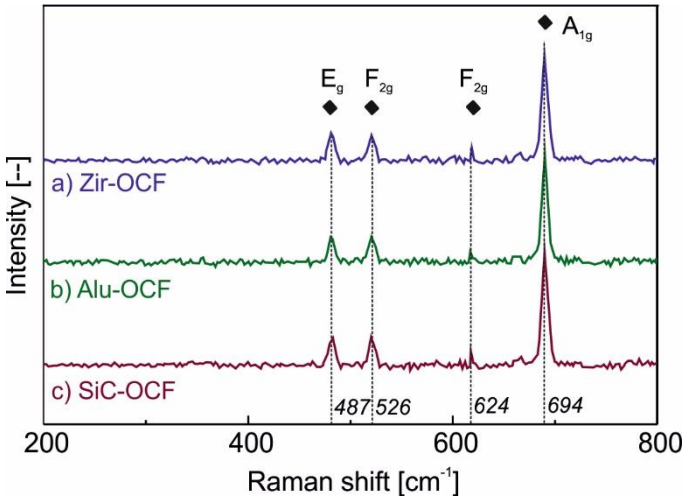

Figure 2. Raman spectra of the three OCF coated with 3% PdO on 200 mg Co_3O_4.

3.2. Catalytic Tests toward CH_4 Combustion

The three OCFs coated with 3 wt.% PdO on 200 mg of Co_3O_4 were tested toward CH_4 combustion in lean conditions at 30 WHSV, feeding two different inlet CH_4 concentrations in the reactor (0.5 and 1.0 vol.%, respectively), as shown in **Figure 3**. All the three types of coated OCFs reach full CH_4 conversion at a temperature below 460 °C, independently on the inlet CH_4 concentration. A higher inlet CH_4 concentration shifts the curves toward slightly higher values of temperature. In all examined cases, Zir-OCF behaves better than Alu-OCF and SiC-OCF, respectively, reaching complete conversion at a temperature below 380 °C. The light-off temperatures (T_{10}, temperature at which the catalyst reached 10% of CH_4 conversion) are very similar for all OCFs, from a minimum of 235 °C for Zir-OCF (0.5% CH_4 inlet) to a maximum of 270 °C for SiC-OCF (1.0% CH_4 inlet). Interestingly, the difference is more evident on light-on temperatures (T_{90}, temperature at which the catalyst reached 90% of CH_4 conversion), which range from a minimum of 323 °C for Zir-OCF (0.5% CH_4 inlet) to a maximum of 392 °C for SiC-OCF (1.0% CH_4 inlet). Both Zir-OCF reach full conversion at a temperature of ≈ 360 °C, while the other two supports at temperatures higher than 410 °C. These results can be explained considering the different values of the thermal conductivity of the three OCFs (listed in **Table**

1). In fact, the lowest thermal conductivity value of Zir-OCF allows reaching complete CH_4 conversion at lower temperature compared to the other supports. As we estimated in our previous works by measuring either in inlet and outlet temperatures during the reaction in different reactive conditions [33,34], the volumetric heat transfer coefficients are increasing with WHSV and decreasing with temperature, following the order Zir-OCF ($2 \cdot 10^4$–$0.5 \cdot 10^5$ W m^{-3} K^{-1}) < Alu-OCF ($1.5 \cdot 10^5$–$9 \cdot 10^5$ W m^{-3} K^{-1}) < SiC-OCF ($2 \cdot 10^5$–$1 \cdot 10^6$ W m^{-3} K^{-1}). These values are in logic agreement with the thermal conductivities values of different monoliths, ceramic and metallic available in the literature [20,85–87]. Moreover, these results are in fully agreement with the results obtained by Sanz et al. [78] and Santos et al. [59], studying the catalytic endo- or exo-thermic reactions on ceramic and metallic monoliths coated with catalysts: the most active structured catalysts are the ceramic ones, which have the lowest values of thermal conductivity, as in our case. Thus, these results confirm the important role of the thermal conductivity in favoring the catalytic reaction.

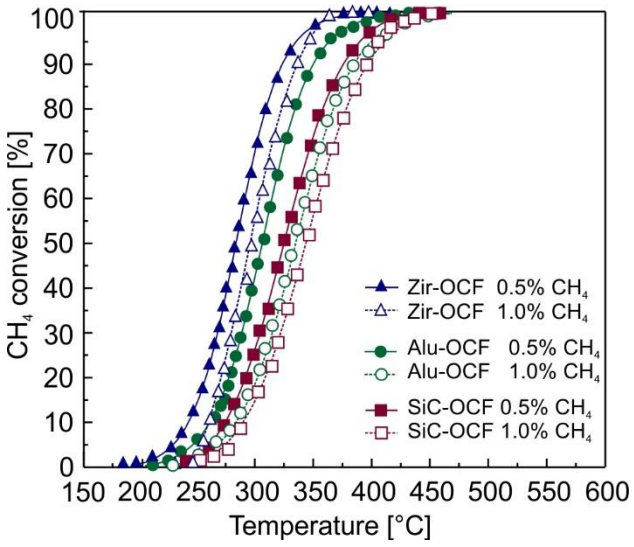

Figure 3. CH_4 conversion versus temperature of the three OCF coated with 3% PdO on 200 mg Co_3O_4, tested at 30 NL h^{-1} g_{cat}^{-1} with two different CH_4 inlet concentrations.

3.3. External and Internal Mass Transfer Limitations

Table 2 provides the catalyst layer thickness of each OCF structure, calculated by assuming that the Pd/Co_3O_4 catalyst is uniformly distributed inside the pores of the OCF and the shape of the catalyst coated layer is circular (see **Figure 4**). As observed, the catalyst thickness increases in the order of Zir-OCF < Alu-OCF < SiC-OCF, maintaining the R_2/R_1 ratio of the coated circular crown approximately equal to 1.1, as proposed by Joshi et al. [60,61] for washcoated monolith.

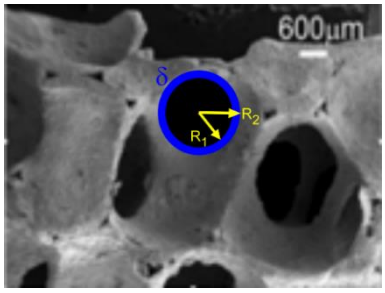

Figure 4. Distribution of the Pd/Co_3O_4 catalyst inside the pore of the OCF with circular coated layer shape.

Table 2. Calculated average catalyst thickness of the OCF catalyst.

OCF material	**Zir**	**Alu**	**SiC**
δ (µm)	46.3	57.7	69.6
R_2/R_1	1.080	1.093	1.094

The evolution of the individual and overall resistances as a function of the temperature is shown in **Figure 5.** As can be noted, the mass transfer resistances ($R_m{}^e, R_m{}^i$) are much less temperature sensitive in comparison to the reaction resistance (R_r), which is strongly dependent on Arrhenius equation. In fact, for the three OCFs studied, the $R_m{}^e$ is nearly independent of temperature. As far as the $R_m{}^i$ is concerned, $R_m{}^i$ is practically invariant at temperatures below 350 and 300 °C for Al- and SiC-OCF catalyst, respectively; while for Zir-OCF catalyst, the $R_m{}^i$ is roughly independent for the entire temperature range studied. Besides, it is also worth noting

that the $R_m{}^i$ becomes more important at lower temperatures for the coated OCFs with higher thermal conductivity and thicker catalytic thickness (Alu- and SiC-OCF, respectively). In particular, the $R_m{}^i$ is more significant for Al-OCF catalyst at temperatures above 400 °C, while for SiC-OCF in the temperature range of 350 to 400 °C, decreasing further as the temperature increases and the $R_m{}^e$ becoming dominant at temperatures above 550°C . On the other hand, since the external resistance to mass transfer is strongly dependent on flow conditions (e.g., temperature, pressure, and superficial gas velocity [88], the three OCF catalysts showed similar values of $R_m{}^e$ (all the catalytic tests were carried out under the same flow conditions). The small difference between the values could be due to the geometrical properties of each OCF such as voidage, pore, and face diameter.

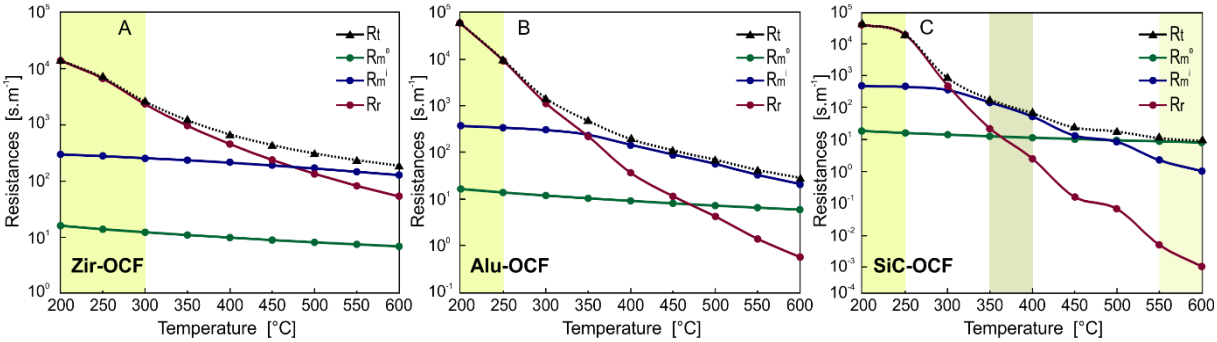

Figure 5. Various resistances for the three OCF catalysts in the process of mass transfer with chemical reaction: A. Zir-OCF, B. Alu-OCF and C. SiC-OCF.

Regarding the kinectic regime, the reaction resistance (R_r) decreases faster for the supports as greater is the thermal conductivity (Alu- and SiC-OCF, respectively). Expectedly, at low temperature the reaction resistance is the largest resistance for all the OCF catalysts. In particular, the R_r becomes more important for Zir-OCF at temperatures below 300 °C, while for Alu- and SiC-OCF at temperature lower than 250 °C. Furthermore, comparing the values of Thiele modulus (ϕ) and efectiveness factors (η) for all the OCFs studied (see **Figure 6. B**), it

can be noticed that the Zir-OCF obtained the lowest values of Thiele modulus ($ø_{max,@600°C} = 3.5$), leading therefore to effectiveness factor values very close to 1, operating the catalytic process in a combination between kinetic ($T < 300°C$; $ø \ll 1$) and transition regime ($T > 300°C$). On the other hand, for Alu- and SiC-OCF, the reaction rate tends to be faster, thus obtaining higher Thiele modulus values, especially for SiC-OCF with $ø > 100$ at temperatures above 550 °C, becoming the diffusion in the dominant process at $T > 350\,°C$. It is also necessary to point out that the R_r is directly dependent on the kinetics of the reaction. Thus, we first calculate the apparent rate constant per unit of the catalyst bulk density (k') for a first-order reaction as :

$$k'(T) = \frac{1}{\tau} \cdot \ln\left(\frac{1}{1-X_{CH4}(T)}\right) \quad (21)$$

$$\tau = \frac{W_{cat} \cdot C_{CH4}^{in}}{F_{CH4}^{in}} \quad (22)$$

where τ is the contact time (g_{cat} s m^{-3}), X_{CH4} is the conversion of methane, W_{cat} is the weight of Pd/Co_3O_4 catalyst (0.2 g_{cat}) and C_{CH4}^{in}, F_{CH4}^{in} are the inlet concentration (mol m^{-3}), and molar flow of methane (mol s^{-1}), respectively.

Then, the k' was plotted as a function of inverse temperature for methane conversions below 10% using the logarithmic form of the Arrhenius equation (see **Figure 6.A**). The activation energy for the three OCF catalyst were found to be 85.95, 107.2 and 191.6 kJ mol^{-1} for Zir-, Alu-, and SiC-OCF, respectively. The kinetic rate constants were given by the following expressions:

$$k_{Zir-OCF} = 2.78 \cdot 10^{-1} \cdot e^{-\frac{10338}{T}} \quad (23)$$

$$k_{Al-OCF} = 3.74 \cdot 10^{4} \cdot e^{-\frac{12897}{T}} \quad (24)$$

$$k_{SiC-OCF} = 2.83 \cdot 10^{12} \cdot e^{-\frac{23052}{T}} \quad (25)$$

As can be observed, lower activation energy values were obtained for Alu- and Zir-OCF. These activation energy values could correspond to the activation energies for the transition and internal diffusive regime (inside the PdO/Co_3O_4 catalyst). In fact, for the entire temperature range studied, the slope of the line corresponding to $-E_a/R$ (obtained by plotting the Arrhenius equation on a logarithmic scale) was practically the same for both OCF structures. On the contrary, for SiC-OCF catalyst, three zones can be distinguished: kinetic regime (at low temperatures with CH_4 conversions lower than 10%), internal diffusion regime (at medium temperatures), where the slope $(-E_a/R)$ corresponds to approximately half of the slope obtained for the kinetic regime $({E_a}^{id} = E_a/2)$, and external diffusion regime (at high temperatures) with ${E_a}^{ed} \approx 0$. Also, as expected, the internal diffusion activation energies $({E_a}^{id})$ for the three coated OCFs showed similar values $(E_{a_{Zir-OCF}}^{id} = 85.95\,\frac{kJ}{mol};\ E_{a_{Al-OCF}}^{id} = 92.4\,\frac{kJ}{mol}\ ;\ E_{a_{SiC-OCF}}^{id} = 86.1\,\frac{kJ}{mol})$.

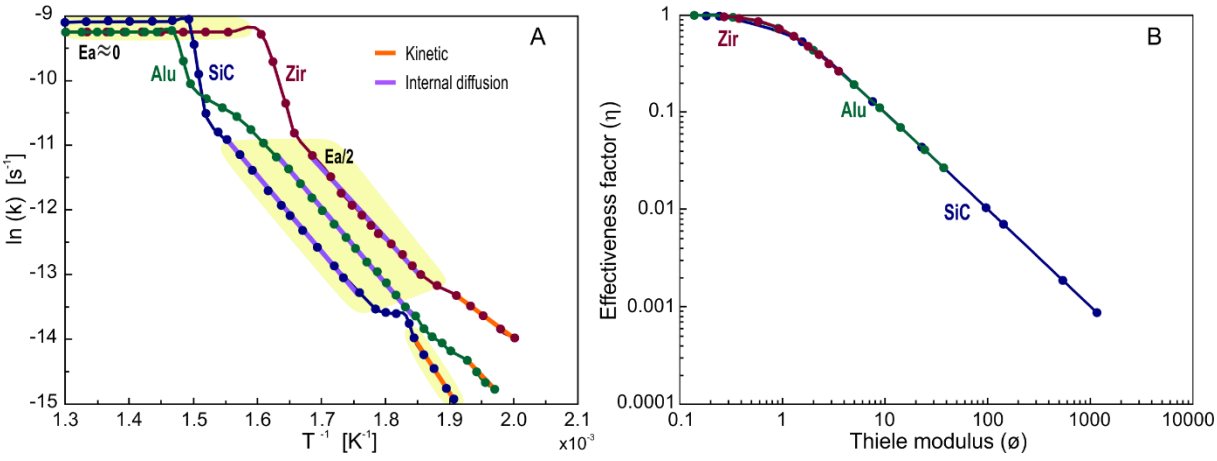

Figure 6. Estimation of rate constant from the experimental data (A) and effectiveness factor vs Thiele modulus for cylindrical geometry (B) for all the OCF catalyst.

3.4. External and Internal Heat Transfer Limitations

According to the criteria developed by Mears (Eq. 13), external heat transfer limitations are present at temperatures approximately above 215, 250, and 242 °C for Zir-, Alu- and SiC-OCF,

respectively (see **Figure 7.A**). These heat effects could be due to the fact that the reaction starts to develop conversions higher than 10% producing more heat due to the exothermicity of the combustion process than the heat removed by the flue gases. Furthermore, analyzing the heat reaction and removal rates as a function of bulk temperature (**Figure 8**), it can be noted that the heat removal (Q) for Zir-OCF is higher than the heat produced by the combustion reaction (Q_r) at bulk temperatures below 400 °C (**Figure 8.A**), reaching the temperature at the catalyst surface T_s ($T_{s,Zir\text{-}OCF}$ = 453 °C; at the steady state condition) in the metastable zone of the heat of reaction curve, for which Q_r is greater than Q (**Figure 8.B**). On the other side, for Alu- and SiC-OCF supports, heat removal is higher than heat production at temperatures lower than 304 and 278 °C, respectively (see **Figure 8.C** and **Figure 8.E**), thus the process is operated in a stable zone reaching the T_s (obtained from the intersection of the Q and Q_r curves, which correspond to the steady state condition) of 317 and 286 °C for Alu- and SiC-OCF, respectively (see **Figure 8.D** and **Figure 8.F**). At higher temperatures, the process performance is in an unstable zone as the heat produced by combustion is greater than the heat removed.

On the contrary, as observed in **Figure 7.B**, no internal heat transfer limitations are observed according to the criterion developed by Anderson (Eq.15), thus confirming the absence of temperature gradients inside the catalytic layer.

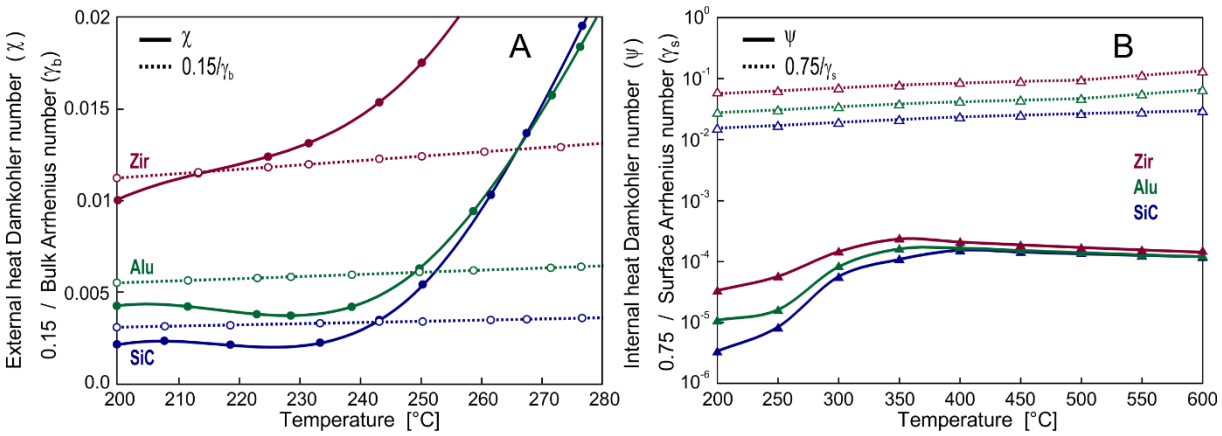

Figure 7. Criteria for evaluating the effects of external heat transfer (A) and internal heat transfer (B) for all the OCF catalyst.

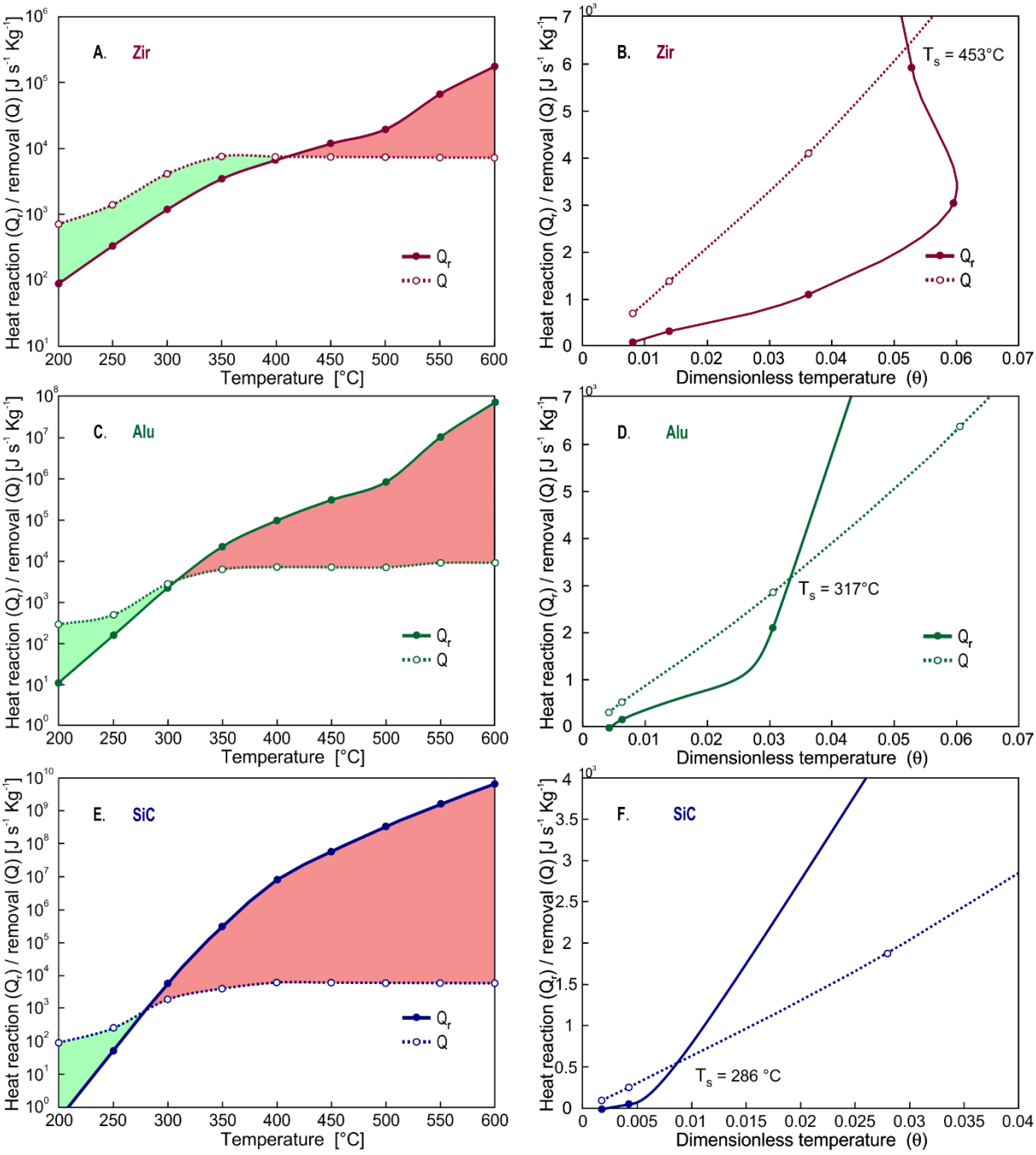

Figure 8. Heat reaction and removal rates as a function of bulk and dimensionless temperatures for Zir-OCF (A/B), Alu-OCF (C/D) and SiC-OCF (E/F).

It is important to remark that the analysis of heat and mass transfer above presented has been conducted by assuming that all pores of the foam are of circular shape, as well as circular is also the shape of the coated layer of catalyst (that is a coated catalyst of constant thickness,

Figure 4). However, as evident from FESEM images (**Figure 1**), most of the foam pores are not perfectly circular, but they have an oval tendency. Thus, the characteristic lengths, both internal and external, vary. To study the effect of the pore shape and catalyst thickness on mass and heat transfer analysis, we performed a comparative analysis of mass and heat transfer for the best structured catalyst that is Zir-OCF, tested in the conditions of inlet CH_4 concentration of 0.5 vol.% and WHSV of 30 NL h^{-1} g_{cat}^{-1}.

We performed a new set of calculations for case-studies assuming the zirconia foam with pores of oval shape instead of circular. More than 50 measurements were performed on FESEM images to determine the average length of the major and minor axis of the pore. For the coated catalyst layer, we considered two alternative cases, shown in **Figure 9B/C**: oval (B) and circular (C) shape of the coated layer (thus, constant or variable thickness for the coated catalyst), while considering the foam pores always oval. These figures are available in an enlarged view in the *Supporting Info S.3* (FESEM Images), **Figures S3.1**, **S3.2**, and **S3.3**.

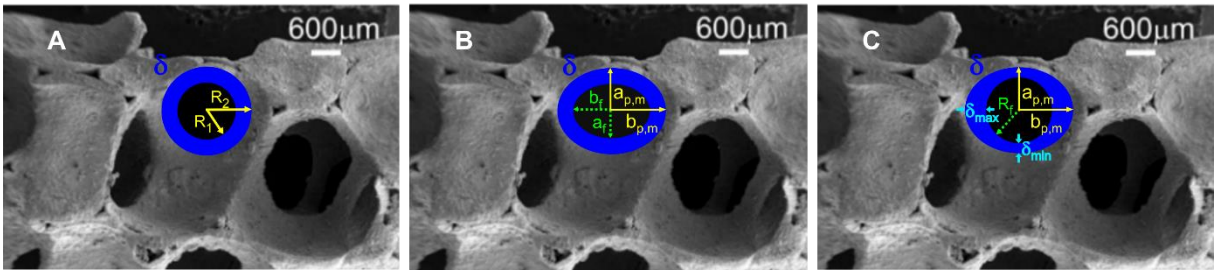

Figure 9. The three different hypothesis considered to evaluate heat and mass transfer on Zir-OCF: case A) circular pore with circular deposition of the catalyst layer; case B) oval pore with oval deposition of the catalyst layer; case C): oval pore with circular deposition of the catalyst layer.

Table 3 shows a comparison of the effect of pore shape and catalyst thickness in terms of predominant resistances (kinetic, internal, and external diffusive) and heat transfer limitations (for 3 wt.% Pd/Co_3O_4 catalyst on Zir-OCF, inlet CH_4 vol.% = 0.5, WHSV 30, temperature range

200-600 °C). As observed, when considering oval both the pore shape and catalyst thickness, the kinetic control prevails at temperatures below 300 °C (see **Fig. S4.2**). As the temperature increases, the reaction rate increases as well, giving rise to a Transition I regime in which the reaction kinetics predominates ($R_r^o >> {R_m}^{i,o}$, ${R_m}^{e,o}$). At temperatures above 476 °C, the reaction rate continues to increase and the concentration in the catalyst thickness decreases. Thus, since the reaction occurs in the catalyst layer, the diffusion limitations begin to appear, and the process moves to a second Transition II regime in which internal diffusion predominates in the combustion process. These results are practically similar to those obtained previously considering of circular shape both the pore and catalyst thickness, with a negligible difference (less than 1%, comparison of **Fig. S4.1** and **S4.2**). Regarding the heat transfer, according to Mears criterion, external heat limitations are observed at temperatures above 233 °C, showing a difference of around 18 °C with respect to the result obtained for circular pore and catalyst layer. On the other hand, the case C), with oval pore and circular catalyst thickness shape, describes the general situation in which the catalyst is deposited preferentially in some areas of the pore, exhibiting a maximum thickness (δ_{max}), while in other areas only a thin layer of catalyst is present in the pore (δ_{min}). As expected, with a greater accumulation of catalyst in some areas of the pore, the performance of the process in terms of predominant resistance is affected, even if not in a considerable and significant way. In this case, the internal diffusive resistance becomes predominant at a temperature above 283 °C, reaching control with respect to ${R_m}^{e,oc}$, and R_r^{oc} at a temperature above 550 °C (see **Fig. S4.3**). Concerning the heat transfer, external heat limitations are observed at a temperature above 261 °C, differing from the circular pore-catalyst layer case of approximately 46 °C. No internal heat transfer limitations were found for any of the cases studied.

Table 3. Comparative heat and mass transfer analysis considering different case studies for the coated Zir-OCF (**Fig. 9**): case A) circular pore with circular deposition of the catalyst layer; case B) oval pore with oval deposition of the catalyst layer; case C): oval pore with circular deposition of the catalyst layer. See *Supporting Info S.4* (Diffusion and kinetic resistances of the cases A, B, and C and related **Figures S4.1**, **S4.2**, and **S4.3**). Reaction conditions: inlet CH_4 concentration of 0.5 vol.% and WHSV of 30 NL h^{-1} g_{cat}^{-1}.

	Pore-coated layer shape (Fig. 9)		
	Circular-Circular A (Fig. S4.1)	Oval-Oval B (Fig. S4.2)	Oval-Circular C (Fig. S4.3)
	Temperature [°C]		
Kinetic control	300 <	300 <	--
Transition I : *Kinetic predomination*	300-474	300-476	200-283
Transition II: *Internal diffusion predomination*	474 >	476 >	283-550
Internal mass transfer control (IMTC)	--	--	550 >
$\chi = \left\lvert \frac{(-\Delta H_r) \cdot R^{obs} \cdot R_{\Omega e}}{h_e \cdot T_b} \right\rvert < \frac{0.15}{\gamma_b}$	215 >	233 >	261 >
$\psi = \left\lvert \frac{(-\Delta H_r \cdot R^{obs} \cdot R_{\Omega i}^2)}{\lambda_e \cdot T_s} \right\rvert < \frac{0.75}{\gamma_s}$	No internal heat transfer		

3.5. Stability measurements

Lastly, on the best selected Zir-OCF with an amount of 200 mg of Co_3O_4 and 3% PdO, we conducted a stability test running the reaction of CH_4 combustion in lean conditions for approximately 250 hours of time on stream (reaction conditions: WHSV 30 NL h^{-1} g_{cat}^{-1} and 0.5 vol. % CH_4 inlet concentration). **Figure 10** shows the comparison of the catalytic activity

of the selected Zir-OCF before and after the stability test, that is in the fresh and aged status. The catalytic activity suffers of a slight worsening, with a shift of the temperature of full CH_4 conversion from 380 to 420 °C. The stability of such a structured catalyst can be considered good. According to the literature, the deactivation of Pd-based catalysts in CH_4 combustion at temperatures below 450 °C, in a fuel lean environment, can be linked with hydroxyl accumulation on the oxide supports [9,47].

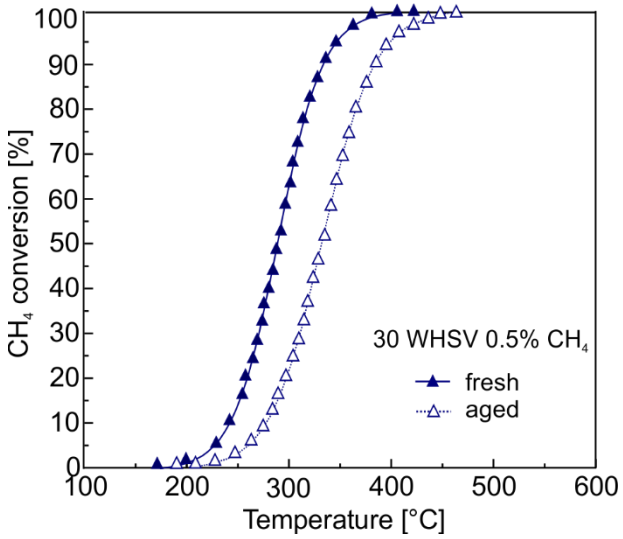

Figure 10. Stability performance: CH_4 conversion versus temperature of the Zir-OCF coated with 3 wt.% PdO on 200 mg Co_3O_4 (tested at 30 NL h^{-1} g_{cat}^{-1} and 0.5 vol. % CH_4 inlet concentration) in the fresh and aged status (after 250 h of time on stream).

Figure 11.A/E show the high angle annular dark field (HAADF) images of the fresh and aged PdO/Co_3O_4 catalyst material extracted from the Zir-OCF before and after the stability test. Due to the inadequate difference in contrast between Pd and Co_3O_4, it was difficult to identify distinct particles of Pd or distinguish between Pd and Co_3O_4 using only Z-contrast in the HAADF images. Therefore, EDXS mapping was used to identify Pd rich regions. The Pd map of the fresh Zir-OCF in **Figure 11.D** shows that Pd rich regions are distributed across the analyzed region, covering in a large and homogeneous extent the surface of the Co_3O_4 spinel (**Fig. 11.B/C**). We do not have specific PdO dispersion data on this structured catalyst, but from

our previous studies on 3% PdO/Co_3O_4 at powder level, the dispersion of PdO was around 30%, which means a high degree of coverage of PdO on the Co_3O_4 spinel [47], which is a results in good agreement this these EXDS mapping of PdO/Co_3O_4 coated on Zir-OCF. From **Figure 11**, EDXS maps of Co and O overlap well with each other in the case of both fresh and aged samples, indicating an absence of Co segregation. However, morphological differences in Co_3O_4 between the fresh and aged samples are evident from the HAADF images. In the case of the fresh sample (**Figure 11.A**), the Co_3O_4 has a rough morphology, as confirmed also by STEM imaging (**Figure 11.B**), while in the aged sample (**Figure 11.E**) it appears to be denser. From EDXS mapping, Co and O distribution in the fresh and aged status remain apparently the same, indicating that Co_3O_4 crystals are preserved, while Pd distribution appears different, not anymore homogeneously distributed after use (**Figure 11.H**), but concentrated in some specific areas. Specifically, **Figure 11.H** indicates local segregation of Pd, with an expected slight reduction of PdO dispersion in the aged catalyst. This also suggests the possibility of particle coarsening, although it is difficult to confirm this directly using these HAADF images due to inadequate contrast. The mobility of Pd, in particular its segregation in areas at high and low Pd concentration could be responsible for the slightly lower performance of the aged catalyst.

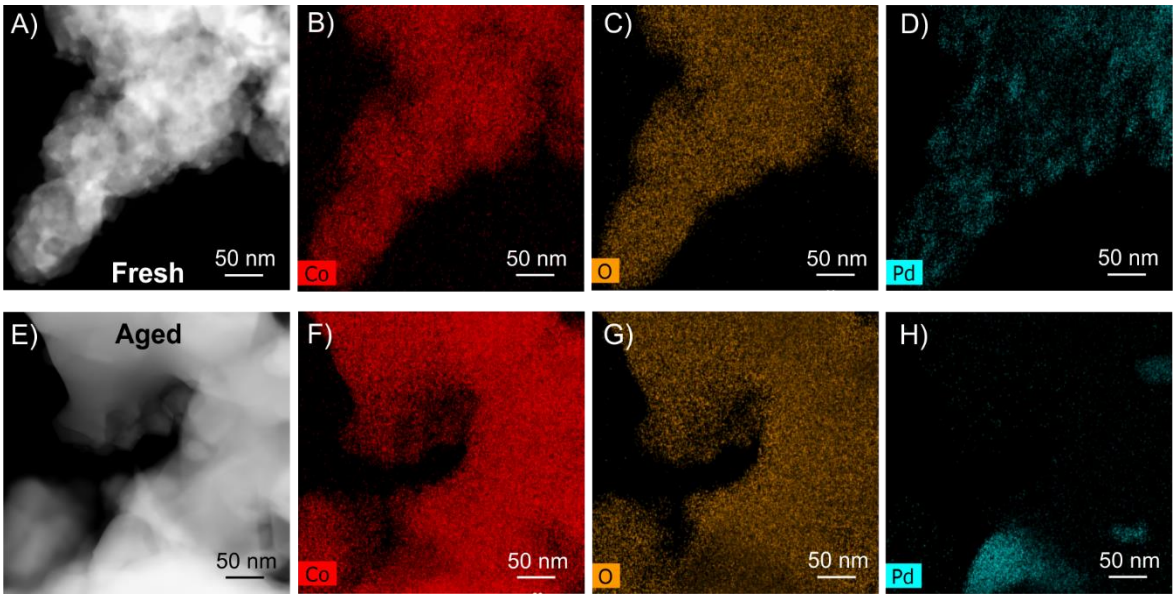

Figure 11. HAADF STEM images and EDXS mappings showing Co, O, and Pd distribution in (**A/B/C/D**) freshly prepared Pd/Co_3O_4 and, (**E/F/G/H**) 250 hours aged Pd/Co_3O_4, collected from Zir-OCF tested in **Figure 10**.

5. Conclusions

The main contribution of this work was to analyze the performance of the 3 wt.% PdO/Co_3O_4 catalyst supported in open cell foams of different ceramic material (zirconia, alumina, and silicon carbide) with 30 ppi for the complete combustion of methane in lean conditions. The Co_3O_4 spinel was deposited by solution combustion synthesis, while the PdO by wetness impregnation. External and internal mass/heat transfer effects were investigated using corroborating theory to determine the apparent kinetics and control regimes of each structured catalyst. The structured catalyst with the wider operative condition is the Zir-OCF, which always displayed temperatures of CH_4 combustion below 380 °C at 30 WHSV. The lowest thermal conductivity value of Zir-OCF allows reaching complete CH_4 conversion at lower temperature compared to the other supports, favoring this highly exothermic reaction. The diffusion inside catalytic layer (internal mass transfer) becomes more important at lower temperatures for the coated OCF with higher thermal conductivity and thicker catalytic thickness (Alu-OCF and SiC-OCF). Because the bulk diffusion (external mass transfer) is strongly dependent on flow conditions, the three OCF catalysts showed similar diffusive values (all tests were carried out at the same flow conditions).

The catalysts investigated, PdO/Co_3O_4, resulted highly stable after approximately 250 hours of operation toward CH_4 combustion in lean conditions. The main suggestion from these results is that for a process intensification requiring high flowrates (that is high WHSV), the use of zirconia OCF with higher values of pore per inches is recommended to avoid external mass-

transfer limitations. These results confirm the important role of the thermal conductivity in favoring the catalytic reaction.

Acknowledgements

This work was performed under the SOL-CARE project (ENERG-065 funded by the Italian Ministry of Education, University and Research – MIUR – through the support of the ERANETMED network). The authors gratefully acknowledge the Global Affairs Office and Office of Vice President for Research of the University of Connecticut (UCONN) for the financial contribution. The STEM studies were performed using the facilities in the UCONN/Thermo Fisher Scientific Center for Advanced Microscopy and Materials Analysis (CAMMA). The FESEM studies were performed using the facilities in the POLITO laboratories (Mr Mauro Raimondo warmly acknowledged). G.E. gratefully acknowledges the financial support of the SOL-CARE project for her stay at UCONN.

References

[1] S.M. Rahman, M.D. Miah, The impact of sources of energy production on globalization: Evidence from panel data analysis, Renew. Sustain. Energy Rev. 74 (2017) 110–115. doi:10.1016/j.rser.2017.02.037.

[2] A. Burnham, J. Han, C.E. Clark, M. Wang, J.B. Dunn, I. Palou-Rivera, Life-cycle greenhouse gas emissions of shale gas, natural gas, coal, and petroleum, Environ. Sci. Technol. 46 (2012) 619–627. doi:10.1021/es201942m.

[3] E.K. Nam, T.E. Jensen, T.J. Wallington, Methane emissions from vehicles, Environ. Sci. Technol. 38 (2004) 2005–2010. doi:10.1021/ES034837G.

[4] N.N. Clark, D.L. McKain, D.R. Johnson, W.S. Wayne, H. Li, V. Akkerman, C. Sandoval, A.N. Covington, R.A. Mongold, J.T. Hailer, O.J. Ugarte, Pump-to-wheels

methane emissions from the heavy-duty transportation sector, Environ. Sci. Technol. 51 (2017) 968–976. doi:10.1021/acs.est.5b06059.

[5] A. Raj, Methane emission control, Johnson Matthey Technol. Rev. 60 (2016) 228–235. doi:10.1595/205651316X692554.

[6] P. Gélin, L. Urfels, M. Primet, E. Tena, Complete oxidation of methane at low temperature over Pt and Pd catalysts for the abatement of lean-burn natural gas fuelled vehicles emissions: Influence of water and sulphur containing compounds, Catal. Today. 83 (2003) 45–57. doi:10.1016/S0920-5861(03)00215-3.

[7] N.M. Kinnunen, J.T. Hirvi, M. Suvanto, T.A. Pakkanen, Methane combustion activity of Pd–PdO_x–Pt/Al_2O_3 catalyst: The role of platinum promoter, J. Mol. Catal. A Chem. 356 (2012) 20–28. doi:10.1016/j.molcata.2011.12.023.

[8] P. Castellazzi, G. Groppi, P. Forzatti, E. Finocchio, G. Busca, Activation process of Pd/Al2O3 catalysts for CH4 combustion by reduction/oxidation cycles in CH4-containing atmosphere, J. Catal. 275 (2010) 218–227. doi:10.1016/j.jcat.2010.07.028.

[9] W.R. Schwartz, L.D. Pfefferle, Combustion of methane over palladium-based catalysts: Support interactions, J. Phys. Chem. C. 116 (2012) 8571–8578. doi:10.1021/jp2119668.

[10] L.F. Liotta, G. Di Carlo, G. Pantaleo, G. Deganello, Catalytic performance of Co_3O_4/CeO_2 and Co_3O_4/CeO_2–ZrO_2 composite oxides for methane combustion: Influence of catalyst pretreatment temperature and oxygen concentration in the reaction mixture, Appl. Catal. B Environ. 70 (2007) 314–322. doi:10.1016/j.apcatb.2005.12.023.

[11] G. Ercolino, P. Stelmachowski, A. Kotarba, S. Specchia, Reactivity of mixed iron–cobalt spinels in the lean methane combustion, Top. Catal. 60 (2017) 1370–1379. doi:10.1007/s11244-017-0826-9.

[12] M.M. Fiuk, A. Adamski, Activity of MnO_x–CeO_2 catalysts in combustion of low concentrated methane, Catal. Today. 257 (2015) 131–135. doi:10.1016/j.cattod.2015.01.029.

[13] S. Specchia, A. Civera, G. Saracco, V. Specchia, Palladium/perovskite/zirconia catalytic premixed fiber burners for efficient and clean natural gas combustion, Catal. Today. 117 (2006) 427–432. doi:10.1016/j.cattod.2006.06.041.

[14] N. Miniajluk, J. Trawczyński, M. Zawadzki, P.E. Tomaszewski, W. Miśta, Solvothermal synthesis and characterization of mixed oxides with perovskite-like structure, Catal. Today. 257 (2015) 26–34. doi:10.1016/j.cattod.2015.03.029.

[15] Y. Wang, H. Arandiyan, J. Scott, M. Akia, H. Dai, J. Deng, K.-F. Aguey-Zinsou, R. Amal, High performance Au–Pd supported on 3D hybrid strontium-substituted lanthanum manganite perovskite catalyst for methane combustion, ACS Catal. 6 (2016) 6935–6947. doi:10.1021/acscatal.6b01685.

[16] A.M. Venezia, V. La Parola, L.F. Liotta, Structural and surface properties of heterogeneous catalysts: Nature of the oxide carrier and supported particle size effects, Catal. Today. 285 (2017) 114–124. doi:10.1016/j.cattod.2016.11.004.

[17] U. Zavyalova, P. Scholz, B. Ondruschka, Influence of cobalt precursor and fuels on the performance of combustion synthesized Co_3O_4/γ-Al_2O_3 catalysts for total oxidation of methane, Appl. Catal. A Gen. 323 (2007) 226–233. doi:10.1016/j.apcata.2007.02.021.

[18] P. Avila, M. Montes, E.E. Miró, Monolithic reactors for environmental applications: A review on preparation technologies, Chem. Eng. J. 109 (2005) 11–36. doi:10.1016/j.cej.2005.02.025.

[19] M. V. Twigg, J.T. Richardson, Fundamentals and applications of structured ceramic foam catalysts, Ind. Eng. Chem. Res. 46 (2007) 4166–4177. doi:10.1021/ie061122o.

[20] E. Tronconi, G. Groppi, C.G. Visconti, Structured catalysts for non-adiabatic

applications, Curr. Opin. Chem. Eng. 5 (2014) 55–67. doi:10.1016/j.coche.2014.04.003.

[21] S. Voltolina, P. Marín, F.V. Díez, S. Ordóñez, Open-cell foams as beds in multiphase reactors: Residence time distribution and mass transfer, Chem. Eng. J. 316 (2017) 323–331. doi:10.1016/j.cej.2017.01.113.

[22] R. Balzarotti, C. Italiano, L. Pino, C. Cristiani, A. Vita, Ni/CeO_2-thin ceramic layer depositions on ceramic monoliths for syngas production by Oxy Steam Reforming of biogas, Fuel Process. Technol. 149 (2016) 40–48. doi:10.1016/j.fuproc.2016.04.002.

[23] M.A. Ashraf, O. Sanz, C. Italiano, A. Vita, M. Montes, S. Specchia, Analysis of Ru/La-Al_2O_3 catalyst loading on alumina monoliths and controlling regimes in methane steam reforming, Chem. Eng. J. 334 (2018) 1792–1807. doi:10.1016/j.cej.2017.11.154.

[24] K. Pangarkar, T.J. Schildhauer, J.R. Van Ommen, J. Nijenhuis, F. Kapteijn, J.A. Moulijn, Structured packings for multiphase catalytic reactors, Ind. Eng. Chem. Res. 47 (2008) 3720–3751. doi:10.1021/ie800067r.

[25] F. García-Moreno, Commercial applications of metal foams: Their properties and production, Materials. 9 (2016) 20–24. doi:10.3390/ma9020085.

[26] Lanik Foam Ceramics, https://www.lanik.eu/en/.

[27] ERG materials & aerospace, http://ergaerospace.com/.

[28] Fraunhofer IFAM, https://www.ifam.fraunhofer.de/content/dam/ifam/en/documents/dd/Infoblätter/open_cell_metal_foams_fraunhofer_ifam_dresden.pdf.

[29] T. Wan, Y. Liu, C. Zhou, X. Chen, Y. Li, Fabrication, properties, and applications of open-cell aluminum foams: A review, J. Mater. Sci. Technol. 62 (2021) 11–24. doi:10.1016/j.jmst.2020.05.039.

[30] I. Švecová, E. Tillová, L. Kuchariková, Improving the quality of Al-Si castings by using ceramic filters, Prod. Eng. Arch. 26 (2020) 19–24. doi:10.30657/pea.2020.26.05.

[31] C. Italiano, M.A. Ashraf, L. Pino, C.W. Moncada Quintero, S. Specchia, A. Vita, Rh/CeO_2 thin catalytic layer deposition on alumina foams: Catalytic performance and controlling regimes in biogas reforming processes, Catalysts. 8 (2018) 1–25. doi:10.3390/catal8100448.

[32] M. Luneau, E. Gianotti, N. Guilhaume, E. Landrivon, F.C. Meunier, C. Mirodatos, Y. Schuurman, Experiments and modeling of methane autothermal reforming over structured Ni–Rh-based Si-SiC foam catalysts, Ind. Eng. Chem. Res. 56 (2017) 13165–13174.

[33] G. Ercolino, P. Stelmachowski, S. Specchia, Catalytic Performance of Pd/Co_3O_4 on SiC and ZrO_2 Open Cell Foams for Process Intensification of Methane Combustion in Lean Conditions, Ind. Eng. Chem. Res. 56 (2017) 6625–6636. doi:10.1021/acs.iecr.7b01087.

[34] G. Ercolino, S. Karimi, P. Stelmachowski, S. Specchia, Catalytic combustion of residual methane on alumina monoliths and open cell foams coated with Pd/Co_3O_4, Chem. Eng. J. 326 (2017) 339–349. doi:10.1016/j.cej.2017.05.149.

[35] O. Sanz, F.J. Echave, M. Sánchez, A. Monzón, M. Montes, Aluminium foams as structured supports for volatile organic compounds (VOCs) oxidation, Appl. Catal. A Gen. 340 (2008) 125–132. doi:10.1016/j.apcata.2008.02.007.

[36] F.C. Patcas, G.I. Garrido, B. Kraushaar-Czarnetzk, CO oxidation over structured carriers: a comparison of ceramic foams, honeycombs and beads, Chem. Eng. Sci. 62 (2007) 3984–3990. doi:10.1016/j.ces.2007.04.039.

[37] L. Giani, G. Groppi, E. Tronconi, Mass-transfer characterization of metallic foams as supports for structured catalysts, Ind. Eng. Chem. Res. 44 (2005) 4993–5002.

doi:10.1021/ie0490886.

[38] A. Aguirre, V. Chandra, E.A.J.F. Peters, J.A.M. Kuipers, M.F. Neira D'Angelo, Open-cell foams as catalysts support: A systematic analysis of the mass transfer limitations, Chem. Eng. J. 393 (2020) 124656. doi:10.1016/j.cej.2020.124656.

[39] G. Pauletto, A. Vaccari, G. Groppi, L. Bricaud, P. Benito, D.C. Boffito, J.A. Lercher, G.S. Patience, FeCrAl as a catalyst support, Chem. Rev. 120 (2020) 7516–7550.

[40] Z. Ren, V. Botu, S. Wang, Y. Meng, W. Song, Y. Guo, R. Ramprasad, S.L. Suib, P.-X. Gao, Monolithically integrated spinel $M_xCo_3{-}xO_4$ (M=Co, Ni, Zn) nanoarray catalysts: scalable synthesis and cation manipulation for tunable low-temperature CH_4 and CO oxidation, Angew. Chemie. 126 (2014) 7351–7355. doi:10.1002/ange.201403461.

[41] I. V. Lukiyanchuk, V.S. Rudnev, I. V. Chernykh, I. V. Malyshev, L.M. Tyrina, M. V. Adigamova, Composites with transition metal oxides on aluminum and titanium and their activity in CO oxidation, Surf. Coatings Technol. 231 (2013) 433–438. doi:10.1016/j.surfcoat.2012.10.031.

[42] J.C. Védrine, I. Fechete, Heterogeneous partial oxidation catalysis on metal oxides, Comptes Rendus Chim. 19 (2016) 1203–1225. doi:10.1016/j.crci.2015.09.021.

[43] B. Farin, A.H.A. Monteverde Videla, S. Specchia, E.M. Gaigneaux, Bismuth molybdates prepared by solution combustion synthesis for the partial oxidation of propene, Catal. Today. 257 (2015) 11–17. doi:10.1016/j.cattod.2015.03.045.

[44] P. Stelmachowski, G. Maniak, J. Kaczmarczyk, F. Zasada, W. Piskorz, A. Kotarba, Z. Sojka, Mg and Al substituted cobalt spinels as catalysts for low temperature deN_2O-Evidence for octahedral cobalt active sites, Appl. Catal. B Environ. 146 (2014) 105–111. doi:10.1016/j.apcatb.2013.05.027.

[45] P. Stelmachowski, K. Ciura, G. Grzybek, Morphology-dependent reactivity of cobalt oxide nanoparticles in N_2O decomposition, Catal. Sci. Technol. 6 (2016) 5554–5560.

doi:10.1039/c6cy00365f.

[46] G. Ercolino, G. Grzybek, P. Stelmachowski, S. Specchia, A. Kotarba, V. Specchia, Pd/Co_3O_4-based catalysts prepared by solution combustion synthesis for residual methane oxidation in lean conditions, Catal. Today. 257 (2015) 66–71. doi:10.1016/j.cattod.2015.03.006.

[47] G. Ercolino, P. Stelmachowski, G. Grzybek, A. Kotarba, S. Specchia, Optimization of Pd catalysts supported on Co_3O_4 for low-temperature lean combustion of residual methane, Appl. Catal. B Environ. 206 (2017) 712–725. doi:10.1016/j.apcatb.2017.01.055.

[48] F. Zasada, W. Piskorz, S. Cristol, J.F. Paul, A. Kotarba, Z. Sojka, Periodic density functional theory and atomistic thermodynamic studies of cobalt spinel nanocrystals in wet environment: Molecular interpretation of water adsorption equilibria, J. Phys. Chem. C. 114 (2010) 22245–22253. doi:10.1021/jp109264b.

[49] F. Zasada, W. Piskorz, Z. Sojka, Cobalt spinel at various redox conditions: DFT+U investigations into the structure and surface thermodynamics of the (100) facet, J. Phys. Chem. C. 119 (2015) 19180–19191. doi:10.1021/acs.jpcc.5b05136.

[50] G. Ercolino, A. Grodzka, G. Grzybek, P. Stelmachowski, S. Specchia, A. Kotarba, The Effect of the preparation method of pd-doped cobalt spinel on the catalytic activity in methane oxidation under lean fuel conditions, Top. Catal. 60 (2017) 333–341. doi:10.1007/s11244-016-0620-0.

[51] A. Varma, A.S. Rogachev, A.S. Mukasyan, S. Hwang, Combustion synthesis of advanced materials: Principles and applications, Adv. Chem. Eng. 24 (1998) 79–226. doi:10.1016/S0065-2377(08)60093-9.

[52] S. Specchia, E. Finocchio, G. Busca, V. Specchia, Combustion Synthesis, Wiley-VCH Verlag GmbH & Co. KGaA, 2010. doi:10.1002/9783527628148.hoc088.

[53] S. Specchia, C. Galletti, V. Specchia, Solution combustion synthesis as intriguing technique to quickly produce performing catalysts for specific applications, Elsevier Masson SAS, 2010. doi:10.1016/S0167-2991(10)75008-4.

[54] A. Varma, A.S. Mukasyan, A.S. Rogachev, K. V. Manukyan, Solution Combustion synthesis of nanoscale materials, Chem. Rev. 116 (2016) 14493–14586. doi:10.1021/acs.chemrev.6b00279.

[55] S. Specchia, G. Ercolino, S. Karimi, C. Italiano, A. Vita, Solution combustion synthesis for preparation of structured catalysts: A mini-review on process intensification for energy applications and pollution control, Int. J. Self-Propagating High-Temperature Synth. 26 (2017) 166–186. doi:10.3103/S1061386217030062.

[56] F. Deganello, A.K. Tyagi, Solution combustion synthesis, energy and environment: Best parameters for better materials, Prog. Cryst. Growth Charact. Mater. 64 (2018) 23–61. doi:10.1016/j.pcrysgrow.2018.03.001.

[57] U.-S. Amjad, C.W. Moncada Quintero, G. Ercolino, C. Italiano, A. Vita, S. Specchia, Methane steam reforming on the Pt/CeO_2 catalyst: Effect of daily start-up and shut-down on long-term stability of the catalyst, Ind. Eng. Chem. Res. 58 (2019) 16395–16406. doi:10.1021/acs.iecr.9b02436.

[58] A. Vita, G. Cristiano, C. Italiano, L. Pino, S. Specchia, Syngas production by methane oxy-steam reforming on Me/CeO_2 (Me=Rh, Pt, Ni) catalyst lined on cordierite monoliths, Appl. Catal. B Environ. 162 (2015) 551–563. doi:10.1016/j.apcatb.2014.07.028.

[59] D.F.M. Santos, O.S.G.P. Soares, J.L. Figueiredo, O. Sanz, M. Montes, M.F.R. Pereira, Preparation of ceramic and metallic monoliths coated with cryptomelane as catalysts for VOC abatement, Chem. Eng. J. 382 (2020) 122923. doi:10.1016/j.cej.2019.122923.

[60] S.Y. Joshi, M.P. Harold, V. Balakotaiah, Overall mass transfer coefficients and

controlling regimes in catalytic monoliths, Chem. Eng. Sci. 65 (2010) 1729–1747. doi:10.1016/j.ces.2009.11.021.

[61] S.Y. Joshi, M.P. Harold, V. Balakotaiah, On the use of internal mass transfer coefficients in modeling of diffusion and reaction in catalytic monoliths, Chem. Eng. Sci. 64 (2009) 4976–4991. doi:10.1016/j.ces.2009.08.008.

[62] S.Y. Joshi, Y. Ren, M.P. Harold, V. Balakotaiah, Determination of kinetics and controlling regimes for H_2 oxidation on Pt/Al_2O_3 monolithic catalyst using high space velocity experiments, Appl. Catal. B Environ. 102 (2011) 484–495. doi:10.1016/j.apcatb.2010.12.030.

[63] V. Balakotaiah, R.R. Ratnakar, On the use of transfer and dispersion coefficient concepts in low-dimensional diffusion-convection-reaction models, Chem. Eng. Res. Des. 88 (2010) 342–361. doi:10.1016/j.cherd.2009.10.008.

[64] G. Incera Garrido, F.C. Patcas, S. Lang, B. Kraushaar-Czarnetzki, Mass transfer and pressure drop in ceramic foams: A description for different pore sizes and porosities, Chem. Eng. Sci. 63 (2008) 5202–5217. doi:10.1016/j.ces.2008.06.015.

[65] L.K.-M. Madhvanand N. Kashid, Albert Renken, Microstructured Devices for Chemical Processing, Wiley-VCH Verlag GmbH & Co. KGaA, 2013. doi:10.1002/9783527685226.

[66] M. Bhattacharya, M.P. Harold, V. Balakotaiah, Mass-transfer coefficients in washcoated monoliths, AIChE J. 50 (2004) 2939–2955. doi:10.1002/aic.10212.

[67] A.K.A. Zeynep Ilsen Onsan, Multiphase Catalytic Reactors, John Wiley & Sons, Hoboker, New Jersey, 2016. doi:10.1002/9781119248491.

[68] J.J. Carberry, Chemical and Catalytic Reaction Engineering, McGraw-Hill, New York, 1976.

[69] D.E. Mears, Diagnostic criteria for heat transport limitations in fixed bed reactors, J.

Catal. 20 (1971) 127–131. doi:10.1016/0021-9517(71)90073-X.

[70] R.P. Chhabra, Fluid Flow and Heat Transfer from Circular and Noncircular Cylinders Submerged in Non-Newtonian Liquids, in: Y.I. Cho, G.A. Greene (Eds.), Adv. Heat Transf. Vol. 43, Elsevier Ltd, 2011: pp. 289–417. doi:10.1016/B978-0-12-381529-3.00004-9.

[71] F.P. Incropera, D.P. DeWitt, Fundamentals of Heat and Mass Transfer, IV, Prentice Hall, Mexico, 1996. doi:10.1016/j.applthermaleng.2011.03.022.

[72] J.B. Anderson, A criterion for isothermal behaviour of a catalyst pellet, Chem. Eng. Sci. 1 (1963) 147–148.

[73] F.C. Buciuman, B. Kraushaar-Czarnetzki, Ceramic Foam monoliths as catalyst carriers. 1. Adjustment and description of the morphology, Ind. Eng. Chem. Res. 42 (2003) 1863–1869. doi:10.1021/ie0204134.

[74] A. Inayat, H. Freund, T. Zeiser, W. Schwieger, Determining the specific surface area of ceramic foams: The tetrakaidecahedra model revisited, Chem. Eng. Sci. 66 (2011) 1179–1188. doi:10.1016/j.ces.2010.12.031.

[75] W.-L. Huo, X.-Y. Zhang, Y.-G. Chen, Y.-J. Lu, W.-T. Liu, X.-Q. Xi, Y.-L. Wang, J. Xu, J.-L. Yang, Highly porous zirconia ceramic foams with low thermal conductivity from particle-stabilized foams, J. Am. Ceram. Soc. 99 (2016) 3512–3515. doi:10.1111/jace.14555.

[76] T. Shimizu, K. Matsuura, H. Furue, K. Matsuzak, Thermal conductivity of high porosity alumina refractory bricks made by a slurry gelation and foaming method, J. Eur. Ceram. Soc. 33 (2013) 3429–3435. doi:10.1016/j.jeurceramsoc.2013.07.001.

[77] T. Fend, B. Hoffschmidt, R. Pitz-Paal, O. Reutter, P. Rietbrock, Porous materials as open volumetric solar receivers: Experimental determination of thermophysical and heat transfer properties, Energy. 29 (2004) 823–833. doi:10.1016/S0360-

5442(03)00188-9.

[78] O. Sanz, I. Velasco, I. Reyero, I. Legorburu, G. Arzamendi, L.M. Gandía, M. Montes, Effect of the thermal conductivity of metallic monoliths on methanolsteam reforming, Catal. Today. 273 (2016) 131–139. doi:10.1016/j.cattod.2016.03.008.

[79] D. Ugues, S. Specchia, G. Saracco, Optimal microstructural design of a catalytic premixed FeCrAlloy fiber burner for methane combustion, Ind. Eng. Chem. Res. 43 (2004) 1990–1998. http://pubs.acs.org/doi/abs/10.1021/ie034202q.

[80] L.C. Almeida, F.J. Echave, O. Sanz, M.A. Centeno, J.A. Odriozola, M. Montes, Washcoating of metallic monoliths and microchannel reactors, in: Stud. Surf. Sci. Catal., 2010: pp. 25–33. doi:10.1016/S0167-2991(10)75004-7.

[81] M.A. Ashraf, O. Sanz, M. Montes, S. Specchia, Insights into the effect of catalyst loading on methane steam reforming and controlling regime for metallic catalytic monoliths, Int. J. Hydrogen Energy. 43 (2018) 11778–11792. doi:10.1016/j.ijhydene.2018.04.126.

[82] V.G. Hadjiev, M.N. Iliev, I. V Vergilov, The Raman spectra of Co_3O_4, J. Phys. C Solid State Phys. 21 (1988) L199–L201. doi:10.1088/0022-3719/21/7/007.

[83] A. Alvarez, S. Ivanova, M.A. Centeno, J.A. Odriozola, Sub-ambient CO oxidation over mesoporous Co_3O_4: Effect of morphology on its reduction behavior and catalytic performance, Appl. Catal. A Gen. 431–432 (2012) 9–17. doi:10.1016/j.apcata.2012.04.006.

[84] P.J. Jodłowski, R.J. Jędrzejczyk, D. Chlebda, M. Gierada, J. Łojewska, In situ spectroscopic studies of methane catalytic combustion over Co, Ce, and Pd mixed oxides deposited on a steel surface, J. Catal. 350 (2017) 1–12. doi:10.1016/j.jcat.2017.03.022.

[85] C.G. Visconti, E. Tronconi, G. Groppi, L. Lietti, M. Iovane, S. Rossini, R. Zennaro,

Monolithic catalysts with high thermal conductivity for the Fischer-Tropsch synthesis in tubular reactors, Chem. Eng. J. 171 (2011) 1294–1307. doi:10.1016/j.cej.2011.05.014.

[86] C.G. Visconti, G. Groppi, E. Tronconi, Accurate prediction of the effective radial conductivity of highly conductive honeycomb monoliths with square channels, Chem. Eng. J. 223 (2013) 224–230. doi:10.1016/j.cej.2013.02.095.

[87] M. Bracconi, M. Ambrosetti, M. Maestri, G. Groppi, E. Tronconi, A fundamental analysis of the influence of the geometrical properties on the effective thermal conductivity of open-cell foams, Chem. Eng. Process. - Process Intensif. 129 (2018) 181–189. doi:10.1016/j.cep.2018.04.018.

[88] H. Scott Fogler, Elements of chemical reaction engineering, 5th ed., Pearson Education, Inc., Kendallville, Indiana (USA), 2016.